Article

Tragacanth, an Exudate Gum as Suitable Aqueous Binder for High Voltage Cathode Material

Daniele Versaci [1,*] **, Oana D. Apostu** [2] **, Davide Dessantis** [3] **, Julia Amici** [1,*] **, Carlotta Francia** [1] **, Marco Minella** [2] **and Silvia Bodoardo** [1]

[1] Electrochemistry Group, Department of Applied Science and Technology, Politecnico di Torino, c.so Duca degli Abruzzi 24, 10129 Torino, Italy

[2] Department of Chemistry and NIS Inter-Departmental Centre, University of Torino, via P. Giuria 5, 10125 Torino, Italy

[3] Synergy of Thermo-chemical and Electro-Chemical Power Systems (STEPS), Department of Energy, Politecnico di Torino, c.so Duca degli Abruzzi 24, 10129 Torino, Italy

* Correspondence: daniele.versaci@polito.it (D.V.); julia.amici@polito.it (J.A.)

Abstract: The improvements in future-generation lithium-ion batteries cannot be exclusively focused on the performance. Other aspects, such as costs, processes, and environmental sustainability, must be considered. Research and development of new active materials allow some fundamental aspects of the batteries to be increased, such as power and energy density. However, one of the main future challenges is the improvement of the batteries' electrochemical performance by using "non-active" materials (binder, current collector, separators) with a lower cost, lower environmental impact, and easier recycling procedure. Focusing on the binder, the main goal is to replace the current fluorinated compounds with water-soluble materials. Starting from these considerations, in this study we evaluate, for the first time, tragacanth gum (TG) as a suitable aqueous binder for the manufacturing process of a cobalt-free, high-voltage lithium nickel manganese oxide (LNMO) cathode. TG-based LNMO cathodes with a low binder content (3 wt%) exhibited good thermal and mechanical properties, showing remarkably high cycling stability with 60% capacity retention after more than 500 cycles at 1 C and an outstanding rate capability of 72 mAh g^{-1} at 15 C. In addition to the excellent electrochemical features, tragacanth gum also showed excellent recycling and recovery properties, making this polysaccharide a suitable and sustainable binder for next-generation lithium-ion batteries.

Keywords: tragacanth gum; binder; high voltage; LNMO; lithium-ion battery; water soluble

1. Introduction

Electrochemical energy-storage systems, such as lithium-ion batteries (LiBs), have turned out to be the most prevalent technology for small electronics, stationary energy-storage applications, and electric mobility. However, to meet the ever-increasing market demand, significant effort is still needed in order to develop batteries with better performance in terms of power and energy density.

Nowadays, it is clear that the battery-performance improvement must go through the development of innovative active materials [1], as well as the constant optimization of the electrodes and cell-manufacturing processes. In fact, it is generally accepted that the performance of a battery is closely linked not only to the electrochemical behaviors of active anode and cathode materials, but also the additional components of the electrode [2].

These additional components of the cell are generally defined as "inactive materials" because they are not directly involved in the electrochemical reactions. The inactive materials include the conductive additive, polymer binders, current collectors, separator, electrolyte, and case/packaging, resulting in approximately 60% of the total weight of a LiB cell. Even though these components are not directly involved in the electrochemical

reaction, they play an important role, determining the battery power and energy density, as well as influencing the cycle and calendar life of the device [3].

Concerning the electrode-manufacturing process, the electrode-slurry optimization has a fundamental impact, not only on the electrochemical performance but also on the sustainability and cost of the whole manufacturing process. For this reason, recently, part of the focus has been shifted toward the study of alternative materials such as new binders [4].

Typically, an ideal binder must ensure a good cohesion between the conductive additive particles and the active material, guaranteeing an optimal adhesion to the current collector. In addition, the binder also has to show high (electro)chemical and thermal stability in the operative voltage range, exhibiting insolubility in the liquid electrolyte and a low swelling phenomenon, without the inhibition of ion transport [5]. Last but not least, a binder can also offer some additional functionalities, such as electronic conductivity and the stabilization of the anode– or cathode–electrolyte interphase (SEI—solid electrolyte interphase and CEI—cathode electrolyte interphase) [4].

Currently, polyvinylidene difluoride (PVdF) is the most common binder, thanks to its good electrochemical and chemical stability and fair processability [6]. Unfortunately, PVdF suffers from some issues, related to both human health and environmental impact. PVdF is synthetized from vinylidene fluoride, which is toxic, irritating to the skin, and highly flammable. At the same time, during the electrode manufacturing, PVdF has to be dispersed into N-methyl-2-pyrrolidone (NMP), which is a mutagenic, teratogenic, and irritating compound [7].

Simultaneously to the health hazards, traditional PVdF/NMP-based electrode manufacturing is 26 times more expensive than an alternative aqueous-based process. In fact, NMP and PVdF are rather expensive (USD $1–3/kg^{-1}$ and USD $8–10/kg^{-1}$, respectively) compared to water and water-soluble polysaccharide compounds (such as carboxymethyl cellulose), which are significantly cheaper (USD $0.015/L^{-1}$ and USD $2–5/kg^{-1}$, respectively) [7]. In addition, concerning the electrode manufacturing, the replacement of an organic solvent such as NMP with water reduces the energy need by more than 40% because the presence of NMP entails an energy-intensive solvent-recovery step [7–10] and takes into account one of the basic principles of green chemistry [11].

For these reasons, in recent years, interest in alternative aqueous binders such as polysaccharides has increased.

In fact, different polysaccharides can be processed in water-based solutions and used as suitable binder for Li-ion batteries thanks to their ability to homogeneous form film on different materials [4]. For example, carboxymethyl cellulose (CMC) has been shown to be a good dispersant in an aqueous medium, especially for anode materials like graphite. CMC is a linear polymeric derivative of cellulose containing different amounts of hydroxyl- and carboxylic-acid functional groups that favor a stable SEI-layer formation [12] and allow for the creation of a crosslinked three-dimensional networks between the particles [5,6]. The role of carboxymethyl cellulose and, in particular, its sodium salt (Na-CMC) was thoroughly investigated in combination with styrene butadiene block co-polymer (SBR) [13] because the coexistence of the two polymers improves the dispersive capability, flexibility, binding strength, and processability of the electrode [5,12]. Thus, the use of the Na-CMC/SBR couple became the state of-the-art approach for aqueous-based processes, especially for anode preparation [7]. Consequently, the great attention being paid to greener manufacturing processes pushes the international research community to investigate many other polysaccharides as alternative binders, especially for graphite- and silicon-based anode electrodes; some examples are sodium alginate (SA) [14–17], gum arabic (GA) [18–21], xanthan gum (XG) [21–23], guar gum (GG) [20,24–28], agar-agar (AA) [29], carrageenan (CG) [29–31], and chitosan [32–36]. Alternative to bio-derived materials, synthetic high-molecular-weight polymers like polyacrylic acid (PAA) [37–42], polyacrylic latex (LA132/133) [43,44], polyvinyl alcohol (PVA) [45–48], and polyacrylonitrile (PAN) [49–51] have also been investigated as binding agents for water-based processes.

Although the use of aqueous binders has become the state of the art for the anode-electrode production, this is not true for cathode electrodes. In fact, the water-based cathode-manufacturing process is still a challenge, in particular for high-voltage cathode electrodes, for which fluorine-based polymers remain the most used binder [7].

For example, lithium nickel manganese oxide (LiNi$_{0.5}$Mn$_{1.5}$O$_4$, LNMO) is one of the most attractive cathode materials for next-generation high-energy-density LiBs. LNMO spinel, unlike other largely used cathode materials such as lithium cobalt oxide (LCO), lithium nickel manganese cobalt oxide (NMC), and lithium nickel cobalt aluminum oxide (NCA), is totally cobalt free, containing only nickel and manganese, with a consequent improvement in terms of cost and eco-political sustainability. Concerning the electrochemical performance, the LNMO theoretical specific capacity is 146.7 mAh g^{-1}, which is lower compared to other commercial cathode materials, but the high energy density is guaranteed by the higher operating voltage (ca. 4.75 V vs. Li/Li$^+$) [52]. This high voltage is one of the main limitations to the use of alternative binders, which have low stability towards oxidation. For example, SBR is not electrochemically stable at higher potentials, meaning that it cannot be used in combination with CMC for LNMO-based electrodes. Additionally, some other side effects, such as lithium leaching and aluminum current-collector corrosion, are directly related to water-based processes, limiting the use of water-soluble binders in industrial cathode manufacturing [53].

Nevertheless, the use of an aqueous CMC binder in an LNMO-based cathode formulation was reported by Wang et al. in 2012 for the first time. In their work, the authors evidenced that the electrodes containing CMC reached higher capacities but lower cyclability compared to electrodes produced using the PVdF/NMP couple. In addition to CMC [54–56], many other studies investigated alternative aqueous binders in LNMO-based electrodes, using, for example, sodium alginate [57–59], guar gum [53], agar-agar [60], carboxymethyl chitosan (CCTS) [61,62], PVAc [63], PAA [59,64], acrylic rubber latex [65], poly(methyl vinyl ether-alt-lithium maleic acid) (P(MVE-LMA) [66], and TRD202A [67]. Some studies focused on the combination of aqueous binders or the addition of crosslinking agents. For example, Kuenzel et al. [53,54] employed natural CMC and GG in the presence of some suitable additives such as phosphoric acid (PA) and adding citric acid (CA) as a natural crosslinker agent. In this case, after adopting CA as crosslinking agent and after 400 cycles, the authors observed a capacity retention of 65% (82 mAh g^{-1}) and 92% (107 mAh g^{-1}) at 1 C for the electrodes containing 5 wt% CMC and 3% GG, respectively. More recently, Rao et al. [59] demonstrated the good mechanical properties and electrochemical performances of LiPAA$-$SA used as composite binder for an LNMO-based cathode. In their study, the electrodes containing the combination of the two binders showed an increased capacity retention of about 93% after 100 cycles at 0.5 C.

In the present study, we selected tragacanth gum (TG) because it is one of the most attractive polysaccharides thanks to its high availability in nature, low cost, and ease of modification based on the different end-use applications [68–72]. In particular, TG is rich in carboxyl and hydroxyl groups, which offer significant opportunities to design its macromolecular structure [68–70]. Last but not least, TG is a biocompatible and biodegradable polymer and is non-toxic for human health [68].

More in detail, among exudate gums, tragacanth is one of the three most important (along with karaya and arabic gums). It comes from a species of Astragalus Gummifer shrub, common in Asian areas (Syria, Turkey, Iran) [71], and its natural form is a complex, highly branched heterogeneous polysaccharide with a total molecular weight of around 840 kDa [68]. Basically, TG consists of two main components: bassorin and tragacanthin [70]. Bassorin represents 60–70% of the total gum. This fraction is insoluble in water but it has a huge swelling capacity, allowing it to form a gel. On the contrary, tragacanthin is soluble in water, resulting in a colloidal, hydrosol solution [73,74]. A small amount of cellulose, starch, protein, and ash is also present in the natural form of TG [69]. Thanks to these properties, tragacanth gum is one of the most used natural gums worldwide, typically

used as stabilizer, thickener, emulsifier, moisturizer, or binding/adhesive agent in many industrial fields (textile, pharmaceutical, food) [68,69,71].

Up to now, the investigation of tragacanth gum as a suitable water-soluble binder employed in the energy-storage industry seems to be limited. In fact, to the best of our knowledge, TG has only been studied as a binder in graphite anodes for LiBs [75] and in carbon-based materials for electrochemical capacitors [76]. Nonetheless, tragacanth gum has never been considered as a binder for high-voltage LNMO-based cathode electrodes.

In the present work, TG was used as a binder in the formulation of an LNMO-based electrode slurry. A low amount of binder (3%) was selected in order to meet the scale-up requirements. The thermal and electrochemical stability of the TG binder was evaluated by means of different techniques. In addition, the electrochemical performance was compared with electrodes using CMC and PVdF as a binder.

2. Materials and Methods

2.1. Thermal, Chemical, and Morphological Characterization

Thermogravimetric analysis (TGA) was conducted on a Linseis TGA PT 1600 instrument with a heating ramp of 10 °C min^{-1} in air from room temperature to 800 °C.

Fourier-transform infrared (FTIR) spectroscopic analysis was performed with a Nicolet^{TM} iS50 FTIR spectrometer (Thermo Scientific^{TM}, Waltham, United States) equipped with an ATR cell from 4000 to 500 cm^{-1} with a resolution of 4 cm^{-1}, and 32 scans were collected.

Field-emission scanning-electron microscope (FESEM) micrographs were collected by a Zeiss SUPRATM 40 with a Gemini column and Schottky field-emission tip (tungsten at 1800 K). Acquisitions were made with magnification up to 1000 KX at an acceleration voltage of 3 kV and a working distance (WD) of 2.1–8.5 mm.

2.2. Slurry Formulation, Electrode Preparation, and Cell Assembly

Commercial LiNi$_{0.5}$Mn$_{1.5}$O$_4$ NANOMYTE$^®$ SP-10 (NEI Corporation, Somerset, NJ, USA) was used as the active material, the conductive additive was carbon black C-NERGY^{TM} Super C45 (Imerys, Paris, France), and the selected binders were sodium carboxymethyl cellulose (Na-CMC, Daicel CMC2200, Hirohata, Japan), tragacanth gum (TG, Sigma–Aldrich, St. Louis, MO, USA), and polyvinylidene fluoride (PVdF Kynar HSV 900, Arkema, Colombes, France).

The positive-electrode composition was set at 92 wt% active material, 5 wt% conductive carbon, and 3 wt% binder.

For the slurry's preparation, CMC and TG were dissolved in deionized water and PVdF in NMP (anhydrous, 99.5%, Sigma–Aldrich, St. Louis, MO, USA) in order to obtain 5 wt% and 8 wt% solutions, respectively.

After complete binder dissolution, carbon black and active material were added and the slurries were homogenized using a ball mill for 15 min at 30 Hz. All the slurries were cast on carbon-coated aluminum foil (MTI, battery grade) using an automated film applicator (Sheen 1133N, speed of 50 mm/s) and a doctor blade (thickness set to 300 μm).

The pH was measured by means of a pHmeter (XS pH 60 DHS) on the pure binder solution (3 wt%) and after the addition of LNMO and carbon black. The pH was monitored for 5 min under magnetic stirring.

The resulting casted/coated electrodes were pre-dried in an oven (Thermo Fisher, Waltham, MA, USA) for 1 h at 80 °C in air. Successively, disks of 1.76 and 0.77 cm^2 (for galvanostatic cycling and the cyclic voltammetry test, respectively) were punched out and vacuum dried at 120 °C (Büchi Glass Oven B-585) for 4 h before cell-assembly. The final electrode-mass loading was set to 6–6.5 mg cm$^{-2.}$

Cells assembly was performed in an Ar-filled glove box (MBraun Labstar, H$_2$O and O$_2$ content < 1 ppm) using a Swagelok-type and Coin cell 2032 for the three- and two-electrode configurations, respectively. Glass fiber (Whatman GF/D) was used as a separator and soaked with an electrolyte solution of LiPF$_6$ 1 M 1:1 *v/v* mixture of ethylene carbonate (EC) and diethyl carbonate (DEC) (Solvionic, Toulouse, France).

LNMO-based cathodes were electrochemically tested against a Li disk that served as a reference and counter electrodes (Ø 10 or 16 mm, thickness 0.6 mm, Tobmachine), between 3.5–4.9 V at RT or at 50 °C, in a dynamic climate chamber (MKF 56, binder).

Cycling performances were assessed through galvanostatic discharge–charge cycling (GC) on an Arbin LBT-21084. Cyclic voltammetry and electrochemical impedance spectroscopy (EIS) characterizations were conducted on a versatile multichannel potentiostat (VMP-3 Biologic, Grenoble, France). Impedance measurements were performed after different cycles of charge–discharge at 0.1 C using a 10 mV amplitude in the 100 kHz–100 mHz frequency range.

2.3. Swelling Test

Swelling of binders was investigated by a simple method [48] in which an equal amount (250 mg) of three different binders (PVdF, Na-CMC, TG) was added to the same volume of electrolyte (0.6 mL). The samples were stored in a vial for 24 h to visually evaluate the interaction between the electrolyte solution and each binder.

2.4. Delamination Test

Electrode delamination was evaluated using an ultrasonic sonication bath (Elmasonic P, Elma, Birmingham, UK) of deionized water for 30 s at 37 Hz.

3. Results and Discussions

The thermal stability of the tragacanth gum was assessed through thermogravimetric analysis (TGA) in air in the range of 25–800 °C.

Figure 1a shows the thermogram of TG: a three-step thermal degradation was observed. The TGA profile displayed a first weight loss of about 8 wt% at around 100 °C, which could be attributed to the adsorbed-humidity release. A second step of weight loss of about 64 wt% was detected in the 230–420 °C range, which was ascribable to the degradation of the highly branched heterogeneous structure of the two fractions of TG [77]. The third step, consisting of the complete oxidation of the polysaccharide [78], occurred in the 420–540 °C range, with a final solid residue of 2.4 wt%.
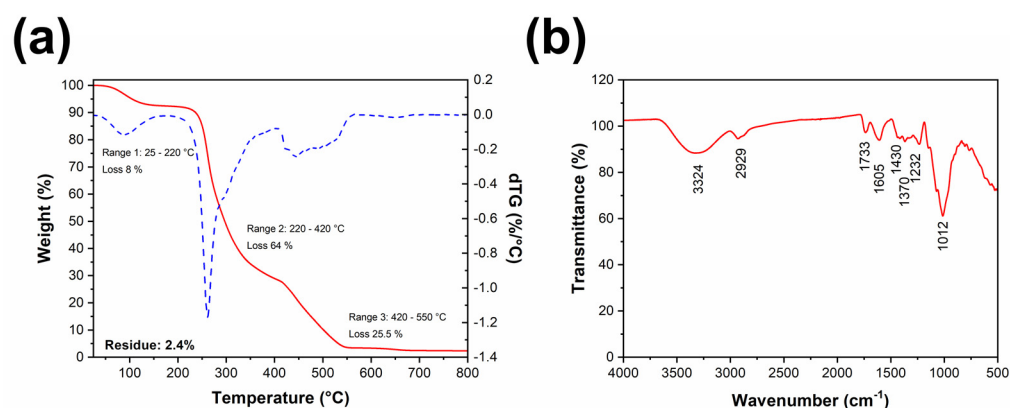

Figure 1. (**a**) Tragacanth gum TGA thermogram (red line) and its first derivative (derivative thermogravimetry (DTG), blue dotted line); (**b**) FTIR spectra of intact tragacanth gum (TG).

This trend confirms that the thermal stability TG is in the traditional LiB operating-temperature range. The thermal stability above 200 °C also means that TG mitigates the risk of electrode damage under working conditions and undesired side reactions, making this binder interesting and useful for electrode preparation.

As previously reported, the functional groups of TG could play a fundamental role to provide not only good adhesion between the active material particles but also worthy elasticity of the electrode. Therefore, to confirm the surface-active properties of TG, a FTIR analysis was performed (see Figure 1b). The broad band observable at 3324 cm^{-1} could

be assigned to a stretching-vibration mode of the –OH group related to inter- and intra-molecular-bound hydroxyl groups and to adsorbed water, whereas the band at 2929 cm^{-1} corresponded to C–H stretching. The peaks at 1733 cm^{-1} could be attributed to asymmetric stretching of C=O in carboxyl groups, whereas the absorption band at 1605 cm^{-1} matched with the asymmetric stretching vibrations of the carboxylate group (–COO−) in galacturonic acid. The peaks between 800 and 1200 cm^{-1} corresponded to the carbohydrate fingerprint, which is the most representative polysaccharide chemical group [79–82].

The abundant presence of hydroxyl and carboxyl groups in TG guarantees a strong interaction between active material and binder but also offers a strong adhesion with the other components of the electrode (carbon black and current collector). For this reason, polysaccharides generally show good binding affinity with LNMO—in particular, thanks to the huge amount of superficial carboxylic and hydroxyl groups able to interact with the oxide-based materials to form a network [53]. On the contrary, PVdF cannot form a uniform coating on LNMO/CB particles, resulting in relevant side reactions on the surfaces in contact with electrolytes, especially at high temperatures and/or high potentials. This behavior generally induces poor CEI stability, an inhomogeneous and thick passivation layer, and consequent marked capacity fading [55].

The electrode mechanical stability is strongly influenced by the interaction with the liquid electrolyte. Indeed, the electrolyte's ability to permeate into the porosity of the electrode guarantees better ion migration and therefore better electrochemical performance. On the contrary, an excessive electrolyte uptake leads to a lower electrode mechanical stability and, as a consequence, lower long-term cycling performance.

Thus, the electrolyte uptake ability of the three different investigated binders was evaluated through a swelling test, as reported in Figure 2. As depicted in Figure 2, PVdF was able to soak-up a larger amount of electrolyte, swelling and forming a gel immediately, whereas TG and CMC were wetted by the electrolyte without showing any evident swelling or gel formation. Additionally, after 24 h (Figure 2b,c), the PVdF remained the only one with the greatest swelling effect.
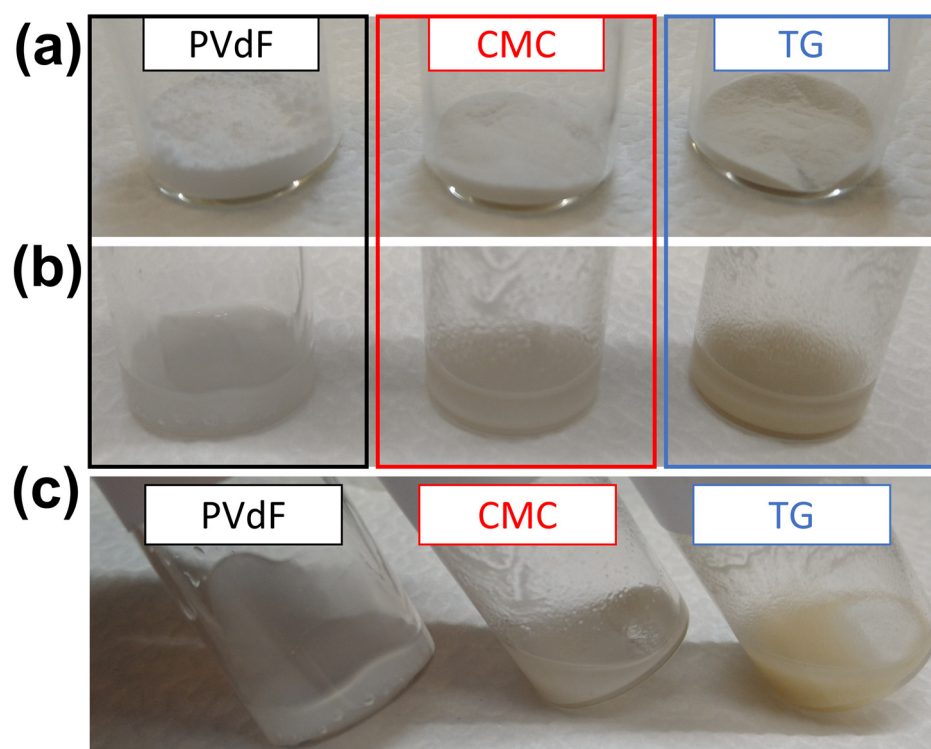

Figure 2. Solubility and swelling test of PVdF, CMC, and TG using LiPF$_6$ 1 M 1:1 *v/v* in EC:DEC electrolyte: (**a**) after electrolyte addition; (**b**,**c**) after 24 h.

The formation of the gel highlights how the electrolyte should easily permeate within the PVdF-based electrode, leading to excessive co-intercalation of the solvent and an expansion of the electrode volume. It is well known that the volume causes electrode exfoliation, which is strongly detrimental for the electronic conductivity, resulting in lower cell electrochemical performance [83].

Therefore, the minor swelling phenomenon observed for TG and CMC suggests an improved mechanical stability of the electrode containing the polysaccharide binders [6,7,13,55].

Concerning the water-based processing of spinels or layered oxide cathode materials, the two major drawbacks are lithium–proton exchange and aluminum current-collector corrosion, which typically occur at high pH values [54,84,85].

Lithium leaching and the concomitant deposition of lithium hydroxide and lithium carbonate inevitably lead to a dense layer formation on the surface of the LNMO-particle surface. At the same time, if the pH moves to basic conditions (pH $\geq$ 9), the dissolution of the aluminum-protective oxide layer starts, with a consequent pitting phenomenon [84].

Therefore, it is essential to control the pH during the slurry-mixing process. Usually, additives such as phosphoric acid or other acids are added to the paste to regulate the pH, making the slurry exploitable for coating. Unfortunately, mild organic-acid addition decreases the pH of the slurry, which inevitably enhances the manganese dissolution [84].

Moreover, the control of the paste pH is mandatory because it can influence the stability of the mixture with consequences for the electrode-coating process and stability.

For these reasons, the pH value was measured for the 5 wt% binder solution before and after the addition of the CB and the AM. The pH value of the 5 wt% TG solution was found to be lower than 6, as expected [72], and rising to less acidic values after the addition of CB and LNMO. However, the paste never reached highly basic pH values (e.g., >8). A similar trend was observed for the CMC, but in this case the starting pH values were slightly higher compared to TG. This means that TG did not negatively alter the pH but allowed the slurry to be kept at controlled pH values and adequately lower than the critical ones.

Subsequently to the chemical–physical analysis of TG, a complete electrode electrochemical characterization was conducted, comparing the behavior of the three different binders. It is worth noting that, to better compare the electrochemical results, the electrode mass loading was kept constant in the range of 6.0–6.5 mg cm^{-2}.

The oxidation stability of the binders was assessed by linear-sweep voltammetry performed using electrodes containing only conductive carbon (CB) and binder, directly deposited on Al foil, and using lithium metal as counter and reference electrodes.

In Figure S1 (see Supplementary Material), the voltammograms of the carbon-black electrodes obtained using PVdF, CMC, and TG as binder are reported. In all cases, no significant anodic current from 2.0 to 5.0 V was observed, indicating stable electrochemical behavior in the operative potential range [61,62]. It is worth noting that at a higher voltage (i.e., >5.5 V), a large anodic current was observed for the CB electrodes containing PVdF, whereas CMC and TG-based electrodes showed lower anodic currents with potential onsets shifted to a higher potential with respect to the PVdF-based electrode. This is in good agreement with previous studies, which revealed an electrolyte-oxidation process on a carbon-black surface at high potentials, with a consequent decrease in carbon electronic conductivity and a higher ionic and electronic barrier within the electrode [64,86–88]. Hence, the CB electrode obtained using CMC and TG as binders showed higher electrochemical stability in liquid organic electrolytes in a wide range of potentials, confirming that polysaccharides provide an effective coating on a CB surface. It is worth noting that a lower reactivity of CB with the electrolyte solutions at high voltages increases the CEI stability of LNMO cathodes [64].

In order to better elucidate the different binders' effect with LNMO, cyclic voltammetry (CV) was carried out at room temperature at a scan rate of 0.1 mV s^{-1} and between 3.0 and 4.9 V (vs. Li/Li$^+$). The cyclic voltammograms of the first 5 cycles for LNMO electrode, marked respectively as LNMO-PVdF, LNMO-CMC, and LNMO-TG, are shown in Figure 3.
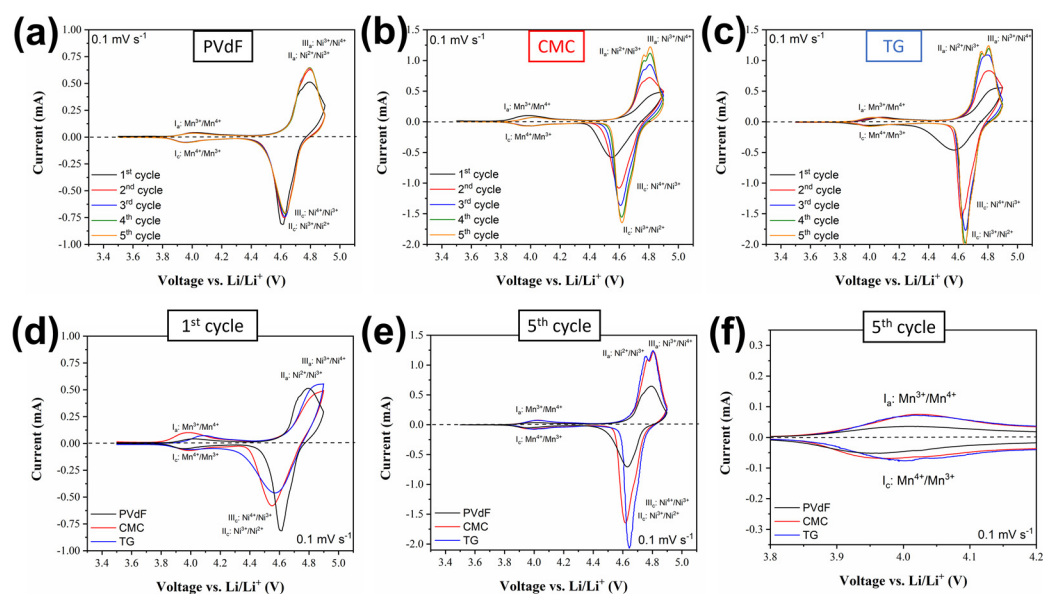
Figure 3. Cyclic voltammetry profiles (0.1 mV s^{-1}) of (**a**) LNMO-PVdF; (**b**) LNMO-CMC; (**c**) LNMO-TG; (**d**) first cycle comparison; (**e**) fifth cycle comparison; (**f**) zoom range of 3.8–4.2 V in the fifth-cycle profile.

All the electrodes displayed a similar CV curve with two sets of redox peaks, typical for LNMO material. As shown in Figure 3a–c, the anode branch of the first cycle showed a first peak of around 4.1 V, which is attributable to the oxidation process of manganese (Mn^{3+} to Mn^{4+}), whereas the less defined peak at around 4.9 V refers to the multiple oxidations of nickel (Ni^{2+}/Ni^{3+} and Ni^{3+}/Ni^{4+}), as widely reported in the literature [52].

In the first anodic branch, the peak related to nickel oxidation showed a marked over-potential, appearing strongly shifted at higher voltage values. This strong polarization was particularly evident for the electrodes containing the aqueous binders (CMC and TG), which consequently showed, in the cathodic branch, a corresponding reduction peak with lower intensity (Figure 3d).

Analyzing the subsequent CV profiles (Figure 3a–c), a progressive decrease in the polarization effect was observable—in particular, for the electrode containing CMC and TG. In fact, for LNMO-CMC and LNMO-TG electrodes, the peaks profiles were more defined as the number of cycles increased, with the possibility of easily identifying the typical two-step reversible nickel-oxidation process. Moreover, the fifth cycle comparison (Figure 3e,f) showed higher redox-current values for electrodes containing aqueous binders, revealing a good reversibility of the redox process.

The voltage hysteresis (ΔV) between the main oxidation and the reduction peaks of manganese (Ia/Ic) and nickel (IIa/IIc) was calculated considering cycle 1 and 5 (Table 1) in order to evaluate the over-potential evolution during cycling.

Table 1. Voltage hysteresis (ΔV) between main oxidation/reduction peaks in CV for the first and the fifth cycle for LNMO-PVdF, LNMO-CMC, and LNMO-TG. Ia/Ic and IIa/IIc refer to the main oxidation and reduction peaks of manganese and nickel, respectively.

		LNMO-PVdF	LNMO-CMC	LNMO-TG
	Peaks	Voltage Hysteresis (ΔV)		
Cycle 1	Ia/Ic	60	0	90
	IIa/IIc	180	355	330
Cycle 5	Ia/Ic	60	40	30
	IIa/IIc	160	190	160

At the first cycle, the ΔV between the anodic and cathodic peaks of the manganese-redox reaction were 60, 0, and 90 mV for the PVdF-, CMC-, and TG-based electrodes, respectively. Meanwhile, the voltage hysteresis for the nickel-redox reaction was lower for the PVdF-based electrode (180 mV) compared to the water-based binder electrodes (355 mV for LNMO-CMC and 330 mV for LNMO-TG).

On the contrary, at the fifth cycle, the peak-to-peak potential separations of nickel-redox couples were strongly decreased, especially for the two aqueous binders. For the TG-based electrode, the ΔV was less than half (160 mV) that of the one calculated at the first cycle, and it was also lower compared to the LNMO-CMC electrode. This means that after a few cycles the polarization observed for the aqueous-based electrodes was strongly reduced, with consequently faster lithium-ion insertion/extraction kinetics and better energy efficiency.

In addition to the voltametric analysis, the effect of the three different binders on the charge-/discharge-cycling performances was assessed within the voltage range of 3.5–5.0 V at 25 °C in a half-cell configuration, using metallic lithium as a counter electrode.

The rate capability of the LNMO electrode containing PVdF, CMC, and TG was performed by gradually increasing the C-rates from 0.1 C to 15 C (note that 1 C corresponded to a charge/discharge rate equal to 146.7 mAh g^{-1} h^{-1}). It is important to note that for higher C-rates (1 C, 5 C, 10 C, and 15 C) the charge current was fixed at 1 C in order not to stress the LNMO material (as reported by the material-specification sheet).

A comparison of the discharge capacity at different C-rates for the three electrodes is reported in Figure 4a. After the three formation cycles at low C-rates (e.g., 0.1 C) the cells were cycled at 0.2 C, showing almost the same performance, with a discharge capacity close to 125–130 mAh g^{-1}, which is only 20 mAh g^{-1} lower than the theoretical one (147 mAh g^{-1}).
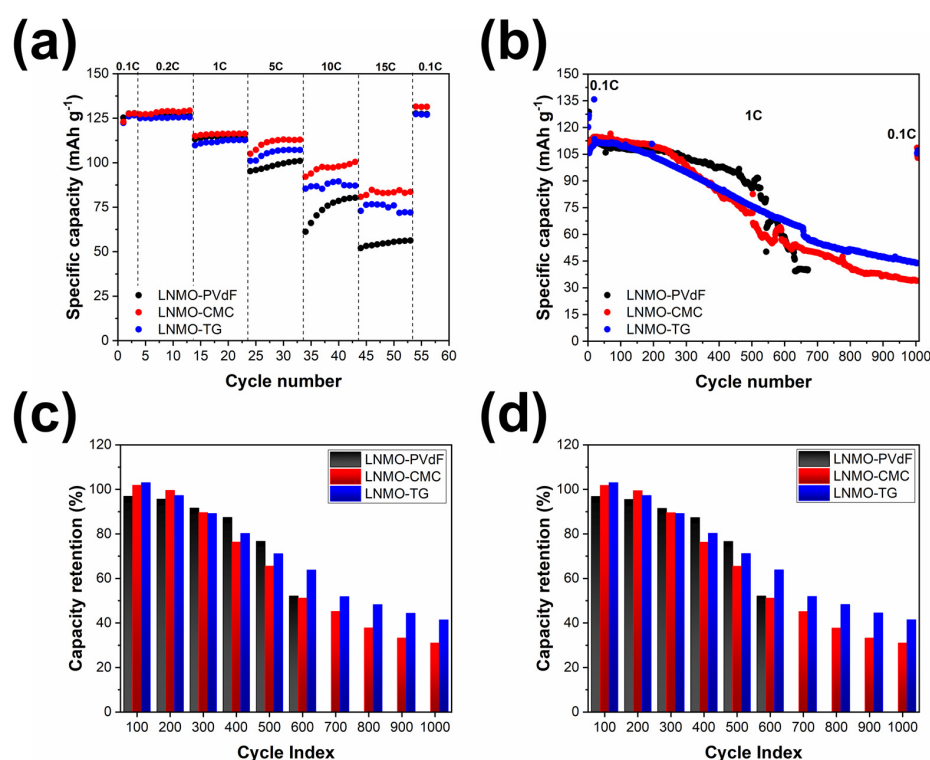

Figure 4. Electrochemical results for half-cell LNMO electrodes containing different binders: (**a**) comparison of the discharge capacity at different C-rates over a wide range of discharge-current densities (0.1–15 C), charge current fixed at 1 C; (**b**) comparison of long-cycling performance (half cells cycled at 0.1 C for 3 cycles and 1 C for further cycles); (**c**) comparison of charge-capacity retention percentiles; (**d**) comparison of discharge-capacity retention percentiles. Cycling at 25 °C between 3.5 V and 4.9 V.

Meanwhile, at rates higher than 1 C, the LNMO-CMC electrode led to a higher practical discharge capacity than LNMO-PVdF and LNMO-TG. However, at 15 C, LNMO-CMC and LNMO-TG electrodes still reached specific capacities of 84 and 72 mAh g^{-1}, respectively, which were significantly higher than the one observed for LNMO-PVdF (56 mAh g^{-1}). At 15 C, the retained specific discharge capacities were 66%, 57%, and 44% for LNMO-CMC, LNMO-TG, and LNMO-PVdF, respectively. When returned back to the 0.1 C rate, the reversible specific capacity of the three electrodes still remained similar to the three initial cycles (Table 2).

Table 2. Summary of discharge-capacity and coulombic-efficiency performance at different C-rates of LNMO electrodes with different binders.

Cycle Number	Discharge Capacity, mAh g^{-1}			Coulombic Efficiency, %		
	PVdF	CMC	TG	PVdF	CMC	TG
1st (0.1 C)	125	122	122	87.3	89.1	88.3
13th (0.2 C)	126	129	125	98.9	97.8	98.8
23rd (1 C)	114	116	112	99.5	99.1	99.5
33rd (5 C)	101	112	107	100.1	99.5	100.0
43rd (10 C)	80	100	87	100.1	99.7	100.0
53rd (15 C)	56	83	72	99.9	99.3	99.2
56th (0.1 C)	127	131	126	98.0	92.9	97.8

Analyzing the coulombic efficiency (CE), it was comparable for the three electrodes, ranging from 87 to 89% in the first cycle at 0.1 C and achieving values higher than 99% by increasing the number of cycles (Table 2). However, returning to the rate of 0.1 C, the coulombic efficiency of LNMO-CMC was lower than 95%, whereas for the other two electrodes it was close to 98%.

It is worth noting that the prepared electrodes were not subjected to a calendaring process, which inevitably affects the microstructures and mechanical properties, as well as the related battery performances, as reported in the literature [59].

To better determine the binder's role inside the electrode formulation the cells were investigated by long-term cycling (up to 1000 cycles at 1 C), and the results are reported and compared in Figure 4b.

The PVdF-based cathode exhibited an initial discharge specific capacity of 125 mAh g^{-1} with a coulombic efficiency of 88.8% at 0. 1 C. At the same time, the CMC-based and TG-based cathodes reached a discharge specific capacity of about 120 mAh g^{-1} (C.E. 84.2%) and 120 mAh g^{-1} (C.E. 88.9%), respectively.

During the three forming cycles at 0.1 C, the specific capacity and the coulombic efficiency of all three samples increased, reaching 129, 127, and 127 mAh g^{-1} for LNMO-PVdF, LNMO-CMC, and LNMO-TG, respectively.

The increase in capacity observed during the initial cycles was probably attributable to the electrode's progressive wetting by the electrolyte solution [89]. This behavior is in good agreement with the CV analysis, in which a relevant polarization phenomenon was present during the first "wetting" cycle.

The voltage hysteresis and the polarization at the first cycle was also evident in the charge/discharge profiles and in the relative dQ/dV curves reported in Figure S2 (see Supplementary Material). In fact, dQ/dV profiles are useful for quantifying the voltage hysteresis during the first cycles.

Comparing the Ni$^{2+/4+}$ redox peak positions, the LNMO-PVdF showed a voltage hysteresis of 148 mV, which was substantially higher compared to the one observed for LNMO-CMC ($\Delta V \sim 62$ mV) and LNMO-TG ($\Delta V \sim 94$ mV), confirming the higher cell impedance for the PVdF-based cathode. Nevertheless, the voltage hysteresis for the subsequent cycles was less than half ($\Delta V \sim 30$–40 mV) for all the cathodes.

After the three initial formation cycles at 0.1 C, the cathodes were tested for 1000 cycles at 1 C (Figure 4b and Figure S3 of Supplementary Material, Table 3). Comparing the fifth

cycle, the three cathodes exhibited a similar specific capacity of about 110 mAh g^{-1}, which was maintained for more than 100 cycles. Moreover, a quick stabilization of the coulombic efficiency of about 99.5% was reached after five cycles.

Table 3. Summary of discharge capacity and coulombic-efficiency performance at different cycles related to a long cycling test of LNMO electrodes with different binders.

Cycle Number	Discharge Capacity			Coulombic Efficiency		
	PVdF	CMC	TG	PVdF	CMC	TG
1st (0.1 C)	126	120	120	88.8	84.2	88.9
2nd (0.1 C)	128	125	125	94.8	97.7	95.3
3rd (0.1 C)	129	127	127	96.6	98.2	96.8
5th (1 C)	112	110	106	99.5	99.6	99.4
100th (1 C)	108	113	110	99.5	99.5	99.4
300th (1 C)	103	98	95	99.4	99.5	99.5
500th (1 C)	86	72	76	99.5	99.5	99.5
700th (1 C)	-	50	55	-	99.5	99.5
900th (1 C)	-	37	47	-	99.5	99.7
1000th (1 C)	-	34	44	-	99.5	99.5

After 300 cycles, approximately 10% of the capacity (calculated in relation to the specific capacity of the fifth cycle) was lost for all the cathodes. As reported in Table 3, the capacity fading was less pronounced for the PVdF-based LNMO electrode up to 540 cycles, at which point the electrode showed a dramatic capacity drop. In sharp contrast, the CMC and TG-based electrodes exhibited a superior cyclability, achieving more than 1000 cycles. The LNMO-TG cathode showed superior capacity retentions starting from the 500th cycle, which appeared substantially higher compared to the CMC-based electrode (up to 1000 cycles).

Returning to the low charge/discharge rates (e.g., 0.1 C) after 1000 cycles, the LNMO-CMC specific capacity was 103 mAh g^{-1}, corresponding to a capacity retention of about 81% (calculated with respect to the third cycle at 0.1 C). At the same time, the final specific capacity of LNMO-TG was 107 mAh g^{-1}, which corresponded to a capacity retention of 84%.

The variations of the capacity retention (in charge and discharge) are presented as a function of cycle number in Figure 4c,d, and the corresponding values are summarized in Table 4. The capacity retention was calculated in relation to the capacity at the fifth cycle (1 C).

Table 4. Summary of capacity-retention percentiles of LNMO electrodes with different binders.

Cycle Number	Capacity Retention (Charge/Discharge) % vs. 5th Cycle (1 C)		
	PVdF	CMC	TG
100th (1 C)	97/97	102/102	103/103
300th (1 C)	92/91	90/90	89/89
500th (1 C)	77/77	66/65	71/71
700th (1 C)	-	45/45	52/52
900th (1 C)	-	33/33	44/44
1000th (1 C)	-	31/31	41/41

The capacity retention after 100 cycles was slightly higher than 100% for the aqueous-based electrodes containing CMC and TG, whereas it is less than 97% for LNMO-PVdF. As the number of cycles increased, the capacity retention decreased for all the electrodes, and after 500 cycles the values were 77, 65, and 71%, respectively, for PVdF, CMC, and TG. After 600 cycles, the LNMO-PVdF cell capacity faded, whereas the capacity retention was around 51% for LNMO-CMC and higher than 60% for LNMO-TG. This difference of about

10% between LNMO-CMC and LNMO-TG was also maintained for the following cycles. After 1000 cycles, the capacity retention was 41% for LNMO-TG and 31% for LNMO-CMC.

This behavior suggests a higher stability for the electrodes containing water-based binders—in particular, for the one containing TG. The higher capacity retention observed at 1 C for LNMO-TG after a huge number of cycles (1000) could be ascribed to a lower electrolyte degradation and lower interaction with CB at high potentials, which reasonably means a more stable CEI layer on LNMO.

After long-term cycling, the cells were disassembled in a glove box and the cathodes were investigated by FESEM in order to evaluate the electrode morphology after 1000 charge/discharge cycles. For a better comparison, FESEM micrographs of LNMO electrodes with different binders before and after cycling are shown in Figure 5.
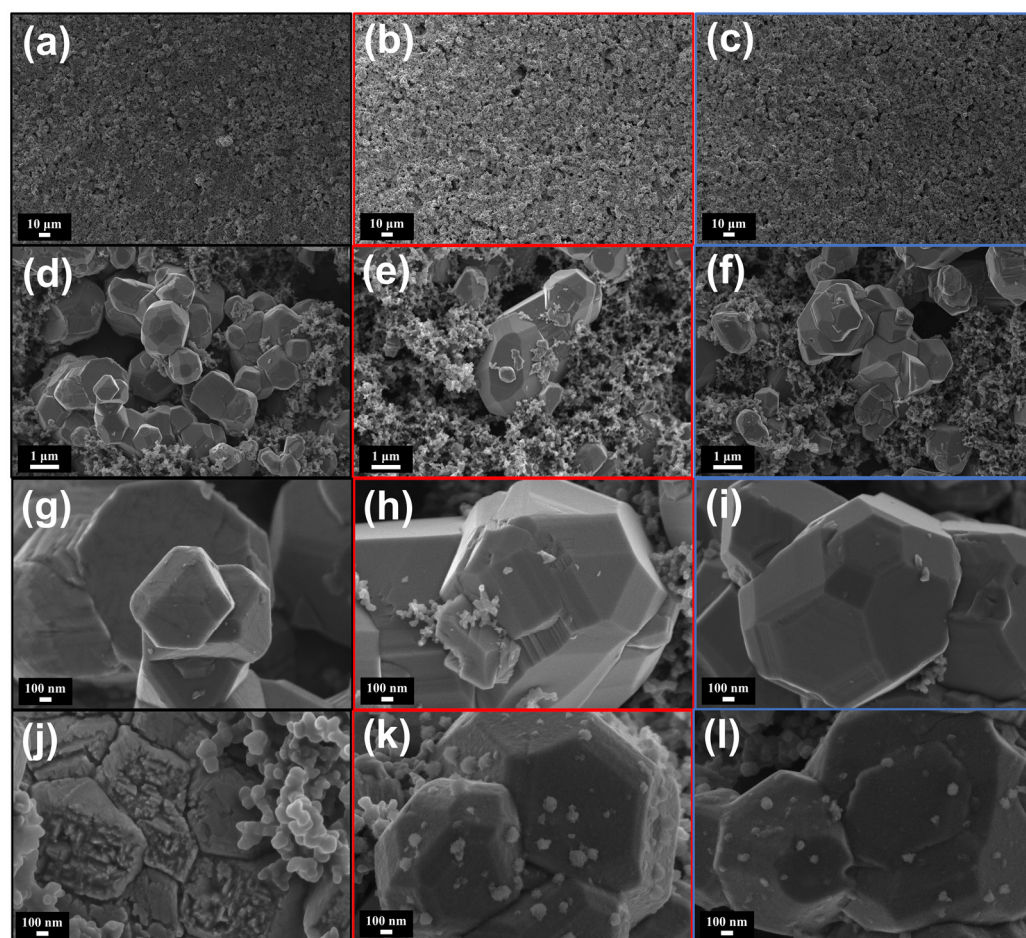
Figure 5. FE-SEM micrographs of pristine and aged cathode electrodes (for 1000 cycles) at different magnifications: (**a,d,g**) pristine LNMO-PVdF electrode; (**b,e,h**) pristine LNMO-CMC electrode; (**c,f,i**) pristine LNMO-TG electrode; (**j**) cycled LNMO-PVdF electrode; (**k**) cycled LNMO-CMC electrode; (**l**) cycled LNMO-TG electrode.

At low magnification (Figure 5a–c), the three electrodes displayed good integrity and a homogeneous distribution of the LNMO and carbon-black particles. The amorphous binders helped maintain a homogeneous distribution of the particles after the drying process [57]. However, discerning the binders' morphologies was quite difficult because the amount inside the electrodes was quite low [58,62]. Reasonably, CMC and TG binders covered the LNMO powder uniformly, which is why it was not possible to discern their presence [57]. On the contrary, the LNMO particles were visible, exhibiting a conventional polyhedron-shaped structure (Figure 5d–i).

Observing the micrographs at higher magnification (Figure 5g–i), the images of pristine LNMO–PVdF clearly showed some micro-cracks on the LNMO-particle surface, whereas for the CMC- and TG-based electrodes no variation was observed (Figure S5 in Supplementary Material). This means that the nature of the binder can also influence the mixing procedure and the preservation of the active-material morphology.

The morphologies of the cycled electrodes (Figure 5j–l) showed a rougher LNMO surface in all samples compared to the uncycled electrodes, but the morphology of the LNMO particles appeared to be damaged for the sample containing PVdF (Figure 5j). In all the electrodes, a visible passivation was the result of the electrolyte decomposition on the surface of the cathode—in particular, at high voltage and after many cycles [55]. In addition, some tiny particles were clearly visible and deposited onto the LNMO surface of the electrodes containing CMC and TG (Figure 5k,l). According to Charles-Blin et al. [90], these particles can be reasonably composed of products originating from the oxidative decomposition of the carbonate-based solvents with $LiPF_6$ salts at the LNMO-cathode surface [91]. It is worth noting that a higher number of small particles was observed on the LNMO-CMC-electrode surface compared to that of the LNMO-TG electrode. This behavior can be directly correlated to the capacity retention, which is higher for TG-based electrodes.

In general, these observations are in line with the electrochemical results, confirming that the degradation of the electrolyte led to lower electrochemical performance upon cycling, which is particularly true for PVdF-based electrodes.

To better clarify the role of the binder on the cycling performance, EIS analysis was carried out on the LNMO-CMC and LNMO-TG electrodes.

EIS measurements were conducted on the pristine electrodes and after different cycles (1st, 2nd, 3rd, 5th, 10th and 50th cycled at 0.1 C).

Observing Figure S4 (see Supplementary Material) for both the electrodes, excluding the profile of the pristine electrode, the Nyquist plots shows two semicircles in the high-to-medium-frequency region and a sloping line in the low-frequency region. As widely reported in previous works [92–94], the initial semicircle, situated in the high-frequency region, can be ascribed to the resistance of the surface film (R_{sf}), whereas the second semicircle (medium-frequency region) is mainly assigned to the charge-transfer resistance (R_{ct}).

All the Nyquist plots, excluding the pristine one, were fitted using the equivalent circuit reported in Figure S4b, and the fitted results are listed in Table S1. More in detail, R_{el} represents the resistance of the electrolyte solution, R_{sf} represents the resistance of the solid-state interface layer formed on the electrode surface, R_{ct} represents the charge-transfer resistance in the electrode/electrolyte interface, and W_o (Warburg element) represents the lithium-ion diffusion in the bulk material [94].

In the Nyquist plot of the pristine electrodes (LNMO-CMC and LNMO-TG) only one semicircle is visible, with a low-resistance R_{el} and a similar resistance to charge transfer for both binders.

After the first cycle at 0.1 C the R_{el} remained approximately constant for both electrodes, whereas a large discrepancy was observed between the R_{sf} and R_{ct}. In fact, the R_{sf} of the LNMO-CMC was about 35 ohm, whereas the one observed for the LNMO-TG was higher, being close to 200 ohm.

At the same time, after the first cycle, the charge-transfer resistance was lower for the CMC-containing electrode compared to that with TG (210 and 362 ohm, respectively).

Observing the subsequent cycles—in particular, those from the second to the tenth, it was possible to identify an evident increasing trend in R_{sf} for the electrode containing CMC. Taking as reference the resistance value observed after the first cycle, the R_{sf} of the CMC-containing electrodes increased over 200% between the first and 10th cycles. Conversely, the surface-film resistance increase was more limited in the electrode containing TG, reaching a maximum of 8%.

In contrast to the R_{sf}, the charge-transfer resistance shows an opposite trend, decreasing as the number of cycles increased. In this case a more marked decrease in the R_{ct} was observed for the electrode containing TG compared to that obtained with CMC. A decrease

close to 70% was observable for LNMO-TG, whereas the reduction in R_{ct} did not exceed 30% for the LNMO-CMC electrode.

In general, it was possible to observe that the R_{sf} of LNMO-TG remained approximately constant during the first 10 cycles, whereas for LNMO-CMC the surface-film resistance increased significantly.

Although the R_{ct} of the two electrodes followed a similar trend, decreasing during the first 10 cycles, it is worth noting that from the second cycle, the charge-transfer resistance of the electrode containing TG became lower than the one of the electrode containing CMC. At the 50th cycle, the surface-film resistance of the two electrodes was comparable, resulting in a range of 50–60 ohm, whereas the charge-transfer resistance of the LNMO-CMC was almost double that of LNMO-TG.

Focusing on the comparison of the surface-film resistance, although it was higher in the electrode containing TG, this value remained almost constant during the first 10 cycles. On the contrary, the R_{sf} of the LNMO-CMC electrode followed a growing trend, suggesting the continuous formation of a layer on the surface of the particles. This layer increased the resistance of the electrode, resulting in a lower conductivity of the lithium ions and limiting the electrochemical kinetics of the system.

The stabilization of the R_{sf} resistance after just one cycle suggests that in the electrode containing TG there was no continuous reaction with the electrolyte during cycling, but there was an immediate stabilization of the surface layer. Conversely, the electrode containing CMC required more time to stabilize. In conclusion, the presence of TG as a binder led to fast stabilization of the cell, limiting the formation of a solid-state interface layer to the first cycles and suppressing the reaction with the electrolyte on the surface of the cathode.

The trend observed for the cell resistances can be related to the results obtained for the long cycling, where the cell containing TG showed a greater cycling ability and a better capacity retention. In this case, a better stabilization of the surface layer of the LNMO particles and of the entire electrode during the first cycles limited the continuous consumption of electrolyte and the formation of thick and highly resistive layers.

The cycling performances of LNMO-CMC and LNMO-TG electrodes were also evaluated under relatively higher-temperature conditions (50 °C), as reported in Figure 6. This test was done because the high temperature could accelerate the capacity decay of the cell and promote the manganese dissolution, the electrolyte decomposition, and the consequent degradation processes.

Both the electrodes with CMC and TG binders showed a stable capacity (close to 115 mAh g^{-1}) after 100 cycles at 50 °C at 1 C. The main difference between the electrodes was observable during the three initial formation cycles, in which the coulombic efficiency of the LNMO-TG electrode appeared to be lower (95%) compared to that of LNMO-CMC (98%). However, after a few cycles at 1 C, the electrodes' specific capacities were similar, with a capacity retention of 93% and 91% after 100 cycles at 1 C for LNMO-CMC and LNMO-TG, respectively. Returning to C/10, no particular electrochemical-performance depletion was detected for the two electrodes, confirming a good and comparable stability of the two polysaccharide binders at high temperature.

Lastly, the recyclability and efficiency of electrode delamination was evaluated using an ultrasound technique [95]. More in detail, the LNMO-TG electrode was submerged in a sonication bath of deionized water for 30 s (37 Hz) and the active material detachment from the current collector was observed. Figure 7 shows the water-based electrode before and after the ultrasonic-bath delamination process.

Thanks to CMC's and TG's good solubility in water, the delamination process was quite fast, and a clean aluminum foil was recovered after few seconds. The good efficacy of this simple process does not suggest the use of more expensive and potentially critical solvents for the recycling of the active material and the current collector. Indeed, the mild condition employed did not affect the aluminum integrity and allowed the active material to be recovered with less time and energy consumption and greener procedures.
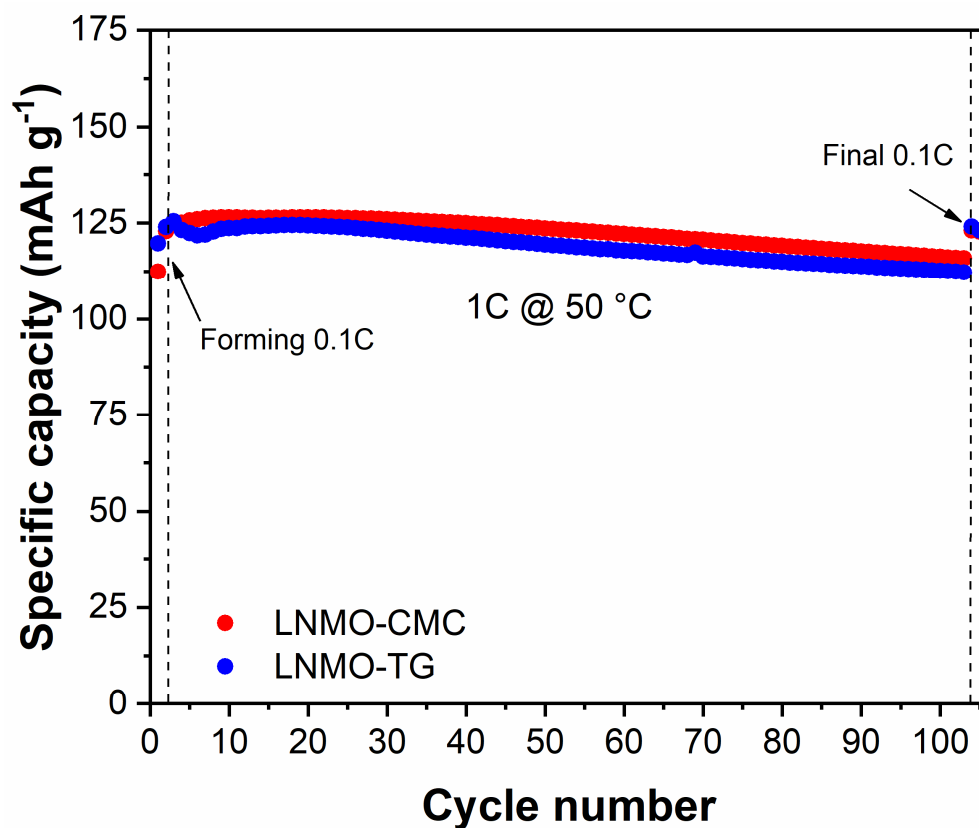
Figure 6. Comparison of specific discharge capacity of the LNMO electrode containing TG and CMC, cycled at 0.1 C for 3 cycles and 1 C for further cycles at 50 °C between 3.5 V and 4.9 V.
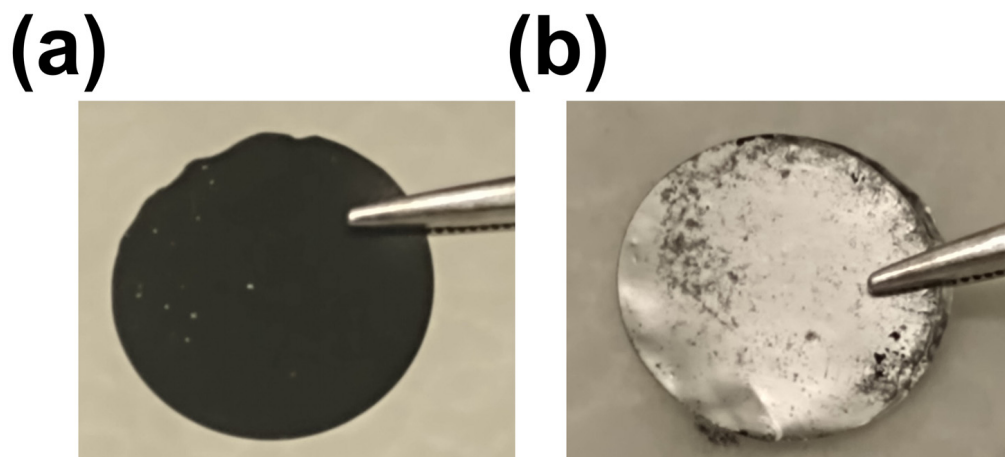

Figure 7. LNMO-TG electrode: (**a**) before; (**b**) after ultrasonic-bath delamination process for 30 s at 37 Hz.

Last but not least, TG was well dispersible in hot or cold water, swelling and originating from a high-viscosity solution [71]. Hence, TG can modify the rheology of aqueous media even at low concentrations (2–3%) [96], showing a viscosity similar to sodium alginate or CMC [72] and shear-thinning behavior [69,71]. This means that the deposition of the electrode slurry is expected to be homogeneous [15,97] and suitable for industrial scaling up.

4. Conclusions

In the present study, tragacanth gum was indagated as an aqueous binder for a high-voltage $LiNi_{0.5}Mn_{1.5}O_4$ spinel cathode, and all results were compared with those obtained using two conventional binders: polyvinylidene-difluoride and carboxy methylcellulose.

More in detail, tragacanth rubber showed high thermal stability up to 200 °C, which makes it suitable in the operating range of common lithium-ion batteries. Meanwhile, the surface chemistry of TG, rich in hydroxyl and carboxyl groups, coupled with its low swelling in contact with the electrolyte, provided better mechanical properties to the electrode.

The LNMO-TG electrodes showed stable electrochemical behavior up to 5.5 V and a progressive decrease in the polarization during the first few cycles, meaning good lithium-ion insertion/extraction kinetics and cyclability.

The electrode containing TG as a binder was able to reach a reversible capacity of 127 mAh g^{-1} at 0.1 C and an impressing-rate capability of 72 mAh g^{-1} at 15 C, with a coulombic efficiency close to 99%.

The most interesting result concerns the long-cycling stability showed by the electrode containing TG, which was investigated here for the first time as binder in a cathode formulation. In fact, LNMO-TG cathodes with 3 wt% binder outperformed PVdF- and CMC-based electrodes. In this case, TG allowed for enhanced cycling stabilities with a capacity retention higher than 60% after 500 cycles, which was significantly higher than those obtained for CMC- and PVdF-based electrodes. TG also showed good mechanical properties and less degradation of the electrode and of the whole system, even after more than 1000 cycles at 1 C and with a high cutoff voltage of 4.9 V. This electrochemical stability, also at a higher temperature (50 °C), could be directly related to the ability of TG to form a stable interphase on the surface of the cathode during the first few cycles, as demonstrated by EIS studies.

Last but not least, TG showed important properties in terms of recovery and recycling, which, together with the electrochemical performance, make tragacanth gum a suitable environmentally friendly and multifunctional binder for next-generation lithium-ion batteries.

Conflicts of Interest: The authors declare that they have no known competing financial interests or personal relationships that could have appeared to influence the work reported in this paper.

References

1. Zhao, Z.; Jiang, X.; Li, S.; Li, L.; Feng, Z.; Lai, H. Microstructure Characterization and Battery Performance Comparison of MOF-235 and TiO_2-P25 Materials. *Crystals* **2022**, *12*, 152. [CrossRef]

2. Heubner, C.; Voigt, K.; Marcinkowski, P.; Reuber, S.; Nikolowski, K.; Schneider, M.; Partsch, M.; Michaelis, A. From Active Materials to Battery Cells: A Straightforward Tool to Determine Performance Metrics and Support Developments at an Application-Relevant Level. *Adv. Energy Mater.* **2021**, *11*, 2102647. [CrossRef]

3. Foreman, E.; Zakri, W.; Hossein Sanatimoghaddam, M.; Modjtahedi, A.; Pathak, S.; Kashkooli, A.G.; Garafolo, N.G.; Farhad, S. A Review of Inactive Materials and Components of Flexible Lithium-Ion Batteries. *Adv. Sustain. Syst.* **2017**, *1*, 1700061. [CrossRef]

4. Zou, F.; Manthiram, A. A Review of the Design of Advanced Binders for High-Performance Batteries. *Adv. Energy Mater.* **2020**, *10*, 2002508. [CrossRef]

5. Schlemmer, W.; Selinger, J.; Hobisch, M.A.; Spirk, S. Polysaccharides for Sustainable Energy Storage—A Review. *Carbohydr. Polym.* **2021**, *265*, 118063. [CrossRef] [PubMed]

6. Cholewinski, A.; Si, P.; Uceda, M.; Pope, M.; Zhao, B. Polymer Binders: Characterization and Development toward Aqueous Electrode Fabrication for Sustainability. *Polymers* **2021**, *13*, 631. [CrossRef] [PubMed]

7. Bresser, D.; Buchholz, D.; Moretti, A.; Varzi, A.; Passerini, S. Alternative Binders for Sustainable Electrochemical Energy Storage—The Transition to Aqueous Electrode Processing and Bio-Derived Polymers. *Energy Environ. Sci.* **2018**, *11*, 3096–3127. [CrossRef]

8. Dühnen, S.; Betz, J.; Kolek, M.; Schmuch, R.; Winter, M.; Placke, T. Toward Green Battery Cells: Perspective on Materials and Technologies. *Small Methods* **2020**, *4*, 2000039. [CrossRef]

9. Wood, D.L.; Li, J.; Daniel, C. Prospects for Reducing the Processing Cost of Lithium Ion Batteries. *J. Power Sources* **2015**, *275*, 234–242. [CrossRef]

10. Gonçalves, R.; Lanceros-Méndez, S.; Costa, C.M. Electrode Fabrication Process and Its Influence in Lithium-Ion Battery Performance: State of the Art and Future Trends. *Electrochem. Commun.* **2022**, *135*, 107210. [CrossRef]

11. Anastas, P.; Eghbali, N. Green Chemistry: Principles and Practice. *Chem. Soc. Rev.* **2010**, *39*, 301–312. [CrossRef]

12. Buqa, H.; Holzapfel, M.; Krumeich, F.; Veit, C.; Novák, P. Study of Styrene Butadiene Rubber and Sodium Methyl Cellulose as Binder for Negative Electrodes in Lithium-Ion Batteries. *J. Power Sources* **2006**, *161*, 617–622. [CrossRef]

13. Lingappan, N.; Kong, L.; Pecht, M. The Significance of Aqueous Binders in Lithium-Ion Batteries. *Renew. Sustain. Energy Rev.* **2021**, *147*, 111227. [CrossRef]

14. Guo, R.; Zhang, S.; Ying, H.; Yang, W.; Wang, J.; Han, W. Preparation of an Amorphous Cross-Linked Binder for Silicon Anodes. *ChemSusChem* **2019**, *12*, 4838–4845. [CrossRef]

15. Toigo, C.; Kracalik, M.; Bradt, E.; Pettinger, K.-H.; Arbizzani, C. Rheological Properties of Aqueous Sodium Alginate Slurries for LTO Battery Electrodes. *Polymers* **2021**, *13*, 3582. [CrossRef] [PubMed]

16. Li, J.; Hu, X.; Zhao, H.; Ren, Y.; Huang, X. Cross-Linked Sodium Alginate-Sodium Borate Hybrid Binders for High-Capacity Silicon Anodes in Lithium-Ion Batteries. *Langmuir* **2022**, *38*, 402–410. [CrossRef] [PubMed]

17. Lai, Y.; Li, H.; Zhang, Y.; Yang, Q.; Li, H.; Sun, Y.; Liu, Y.; Zhong, B.; Wu, Z.; Guo, X. Investigation of Effective Bonding between Varied Binders and Si Anode with Different Particle Sizes. *Appl. Phys. Lett.* **2022**, *121*, 183901. [CrossRef]

18. Ling, M.; Xu, Y.; Zhao, H.; Gu, X.; Qiu, J.; Li, S.; Wu, M.; Song, X.; Yan, C.; Liu, G.; et al. Dual-Functional Gum Arabic Binder for Silicon Anodes in Lithium Ion Batteries. *Nano Energy* **2015**, *12*, 178–185. [CrossRef]

19. Zhong, H.; He, J.; Zhang, L. Crosslinkable Aqueous Binders Containing Arabic Gum-Grafted-Poly (Acrylic Acid) and Branched Polyols for Si Anode of Lithium-Ion Batteries. *Polymer* **2021**, *215*, 123377. [CrossRef]

20. Li, S.; Wu, Z.G.; Liu, Y.M.; Yang, Z.W.; Wang, G.K.; Liu, Y.X.; Zhong, Y.J.; Song, Y.; Zhong, B.H.; Guo, X.D. A Compared Investigation of Different Biogum Polymer Binders for Silicon Anode of Lithium-Ion Batteries. *Ionics* **2021**, *27*, 1829–1836. [CrossRef]

21. He, J.; Zhang, L.; Zhong, H. Enhanced Adhesion and Electrochemical Performance of Si Anodes with Gum Arabic Grafted Poly(Acrylic Acid) as a Water-Soluble Binder. *Polym. Int.* **2021**, *70*, 1668–1679. [CrossRef]

22. Zhang, L.; Jiao, X.; Feng, Z.; Li, B.; Feng, Y.; Song, J. A Nature-Inspired Binder with Three-Dimensional Cross-Linked Networks for Silicon-Based Anodes in Lithium-Ion Batteries. *J. Power Sources* **2021**, *484*, 229198. [CrossRef]

23. Chen, Y.; Gong, Z.; Liu, J.; Gan, L.; Lin, L. Investigation of the Different Structures of Xanthan Gum on the Performance of Silicon Anodes in Lithium-Ion Batteries. *J. Phys. Chem. Solids* **2022**, *165*, 110656. [CrossRef]

24. Carvalho, D.V.; Loeffler, N.; Hekmatfar, M.; Moretti, A.; Kim, G.T.; Passerini, S. Evaluation of Guar Gum-Based Biopolymers as Binders for Lithium-Ion Batteries Electrodes. *Electrochim. Acta* **2018**, *265*, 89–97. [CrossRef]

25. Wang, Z.; Huang, T.; Yu, A. A Carboxymethyl Vegetable Gum as a Robust Water Soluble Binder for Silicon Anodes in Lithium-Ion Batteries. *J. Power Sources* **2021**, *489*, 229530. [CrossRef]

26. Zhao, E.; Guo, Z.; Liu, J.; Zhang, Q.; Guo, Z.; Yang, Y.; Wang, H.; Wang, L. A Low-Cost and Eco-Friendly Network Binder Coupling Stiffness and Softness for High-Performance Li-Ion Batteries. *Electrochim. Acta* **2021**, *387*, 138491. [CrossRef]

27. Kaur, S.; Santra, S. Application of Guar Gum and Its Derivatives as Green Binder/Separator for Advanced Lithium-Ion Batteries. *ChemistryOpen* **2022**, *11*, e202100209. [CrossRef] [PubMed]

28. Padil, V.V.T.; Cheong, J.Y. Recent Advances in the Multifunctional Natural Gum-Based Binders for High-Performance Rechargeable Batteries. *Energies* **2022**, *15*, 8552. [CrossRef]

29. Cuesta, N.; Ramos, A.; Cameán, I.; Antuña, C.; García, A.B. Hydrocolloids as Binders for Graphite Anodes of Lithium-Ion Batteries. *Electrochim. Acta* **2015**, *155*, 140–147. [CrossRef]

30. Li, Z.; Wan, Z.; Wu, G.; Wu, Z.; Zeng, X.; Gan, L.; Liu, J.; Wu, S.; Lin, Z.; Gao, X.; et al. A Biopolymer Network for Lean Binder in Silicon Nanoparticle Anodes for Lithium-Ion Batteries. *Sustain. Mater. Technol.* **2021**, *30*, e00333. [CrossRef]

31. Jang, W.; Rajeev, K.K.; Thorat, G.M.; Kim, S.; Kang, Y.; Kim, T.H. Lambda Carrageenan as a Water-Soluble Binder for Silicon Anodes in Lithium-Ion Batteries. *ACS Sustain. Chem. Eng.* **2022**, *10*, 12620–12629. [CrossRef]

32. Lee, S.H.; Lee, J.H.; Nam, D.H.; Cho, M.; Kim, J.; Chanthad, C.; Lee, Y. Epoxidized Natural Rubber/Chitosan Network Binder for Silicon Anode in Lithium-Ion Battery. *ACS Appl. Mater. Interfaces* **2018**, *10*, 16449–16457. [CrossRef]

33. Rajeev, K.K.; Kim, E.; Nam, J.; Lee, S.; Mun, J.; Kim, T.H. Chitosan-Grafted-Polyaniline Copolymer as an Electrically Conductive and Mechanically Stable Binder for High-Performance Si Anodes in Li-Ion Batteries. *Electrochim. Acta* **2020**, *333*, 135532. [CrossRef]

34. Rajeev, K.K.; Jang, W.; Kim, S.; Kim, T.H. Chitosan- Grafted-Gallic Acid as a Nature-Inspired Multifunctional Binder for High-Performance Silicon Anodes in Lithium-Ion Batteries. *ACS Appl. Energy Mater.* **2022**, *5*, 3166–3178.

35. Liao, H.; Liu, N.; He, W.; Long, J.; Dou, H.; Zhang, X. Three-Dimensional Cross-Linked Binder Based on Ionic Bonding for a High-Performance SiOxAnode in Lithium-Ion Batteries. *ACS Appl. Energy Mater.* **2022**, *5*, 4788–4795. [CrossRef]

36. Wu, Z.; Wan, Z.; Li, Z.; Du, Q.; Wu, T.; Cao, J.; Ling, M.; Liang, C.; Tan, Y. Partially Carbonized Polymer Binder with Polymer Dots for Silicon Anodes in Lithium-Ion Batteries. *Small* **2022**, *19*, 2205065. [CrossRef]

37. Zheng, F.; Tang, Z.; Lei, Y.; Zhong, R.; Chen, H.; Hong, R. PAAS-β-CDp-PAA as a High-Performance Easily Prepared and Water-Soluble Composite Binder for High-Capacity Silicon Anodes in Lithium-Ion Batteries. *J. Alloys Compd.* **2023**, *932*, 167666. [CrossRef]

38. Jing, J.; Zhang, C.; Li, Q.; Li, C.; Yao, S.; Li, T.; Bai, X. Study of Commercial Binders on the Lithium Storage Performance of SiOx/G@C Anode. *Mater. Chem. Phys.* **2022**, *292*, 126797. [CrossRef]

39. Li, Z.; Tang, W.; Yang, Y.; Lai, G.; Lin, Z.; Xiao, H.; Qiu, J.; Wei, X.; Wu, S.; Lin, Z. Engineering Prelithiation of Polyacrylic Acid Binder: A Universal Strategy to Boost Initial Coulombic Efficiency for High-Areal-Capacity Si-Based Anodes. *Adv. Funct. Mater.* **2022**, *32*, 2206615. [CrossRef]

40. Li, Z.; Guo, A.; Liu, D. Water-Soluble Conductive Composite Binder for High-Performance Silicon Anode in Lithium-Ion Batteries. *Batteries* **2022**, *8*, 54. [CrossRef]

41. Su, T.T.; Ren, W.F.; Yuan, J.M.; Wang, K.; Chi, B.Y.; Sun, R.C. Fabrication of Polyacrylic Acid-Based Composite Binders with Strong Binding Forces on Copper Foils for Silicon Anodes in Lithium-Ion Batteries. *J. Ind. Eng. Chem.* **2022**, *109*, 521–529. [CrossRef]

42. Lin, S.; Wang, F.; Hong, R. Polyacrylic Acid and β-Cyclodextrin Polymer Cross-Linking Binders to Enhance Capacity Performance of Silicon/Carbon Composite Electrodes in Lithium-Ion Batteries. *J. Colloid Interface Sci.* **2022**, *613*, 857–865. [CrossRef]

43. Zhong, H.; Sun, M.; Li, Y.; He, J.; Yang, J.; Zhang, L. The Polyacrylic Latex: An Efficient Water-Soluble Binder for LiNi$_{1/3}$Co$_{1/3}$Mn$_{1/3}$O$_2$ Cathode in Li-Ion Batteries. *J. Solid State Electrochem.* **2016**, *20*, 1–8. [CrossRef]

44. Su, M.; Liu, S.; Wan, H.; Dou, A.; Liu, K.; Liu, Y. Effect of Binders on Performance of Si/C Composite as Anode for Li-Ion Batteries. *Ionics* **2018**, *25*, 2103–2109. [CrossRef]

45. Zhao, J.; Wei, D.; Wang, J.; Yang, K.; Wang, Z.; Chen, Z.; Zhang, S.; Zhang, C.; Yang, X. Inorganic Crosslinked Supramolecular Binder with Fast Self-Healing for High Performance Silicon Based Anodes in Lithium-Ion Batteries. *J. Colloid. Interface Sci.* **2022**, *625*, 373–382. [CrossRef] [PubMed]

46. Wang, W.; Li, Y.; Wang, Y.; Huang, W.; Lv, L.; Zhu, G.; Qu, Q.; Liang, Y.; Zheng, W.; Zheng, H. A Novel Covalently Grafted Binder through In-Situ Polymerization for High-Performance Si-Based Lithium-Ion Batteries. *Electrochim. Acta* **2021**, *400*, 139442. [CrossRef]

47. Liu, S.; Zhang, L. Partially Lithiated Ternary Graft Copolymer with Enhanced Elasticity as Aqueous Binder for Si Anode. *J. Appl. Polym. Sci.* **2021**, *138*, 49950. [CrossRef]

48. He, J.; Zhang, L. Polyvinyl Alcohol Grafted Poly (Acrylic Acid) as Water-Soluble Binder with Enhanced Adhesion Capability and Electrochemical Performances for Si Anode. *J. Alloys Compd.* **2018**, *763*, 228–240. [CrossRef]

49. Li, X.Z.; Yuan, S.X.; Ding, G.S. A Comparative Investigation of Various Binders for Silicon Anodes: Interactions with Other Components, Rheological Property, and Behavior in Operando Dilatometry. *Macromol. Mater. Eng.* **2022**, *307*, 2200376. [CrossRef]

50. Yang, Z.; Song, H.; Chen, J.; Lin, K.; Cai, Q.; Li, T.; Zhao, D.; Liu, M.; Qin, X.; Kang, F.; et al. Free-Standing Stable Silicon-Based Anode with Exceptional Flexibility Realized by a Multifunctional Structure Design in Multiple Dimensions. *ACS Appl. Mater. Interfaces* **2022**, *14*, 46439–46448. [CrossRef]

51. Verdier, N.; el Khakani, S.; Lepage, D.; Prébé, A.; Aymé-Perrot, D.; Dollé, M.; Rochefort, D. Polyacrylonitrile-Based Rubber (HNBR) as a New Potential Elastomeric Binder for Lithium-Ion Battery Electrodes. *J. Power Sources* **2019**, *440*, 227111. [CrossRef]

52. Synthesis, Modification, and Lithium-Storage Properties of Spinel LiNi$_{0.5}$Mn$_{1.5}$O$_4$. Available online: https://chemistry-europe.onlinelibrary.wiley.com/doi/epdf/10.1002/celc.202001414 (accessed on 16 January 2023).

53. Kuenzel, M.; Choi, H.; Wu, F.; Kazzazi, A.; Axmann, P.; Wohlfahrt-Mehrens, M.; Bresser, D.; Passerini, S. Co-Crosslinked Water-Soluble Biopolymers as a Binder for High-Voltage LiNi$_{0.5}$Mn$_{1.5}$O$_4$ | Graphite Lithium-Ion Full Cells. *ChemSusChem* **2020**, *13*, 2650–2660. [CrossRef]

54. Kuenzel, M.; Bresser, D.; Diemant, T.; Carvalho, D.V.; Kim, G.T.; Behm, R.J.; Passerini, S. Complementary Strategies Toward the Aqueous Processing of High-Voltage LiNi$_{0.5}$Mn$_{1.5}$O$_4$ Lithium-Ion Cathodes. *ChemSusChem* **2018**, *11*, 562–573. [CrossRef] [PubMed]

55. de Giorgio, F.; Laszczynski, N.; von Zamory, J.; Mastragostino, M.; Arbizzani, C.; Passerini, S. Graphite//LiNi$_{0.5}$Mn$_{1.5}$O$_4$ Cells Based on Environmentally Friendly Made-in-Water Electrodes. *ChemSusChem* **2017**, *10*, 379–386. [CrossRef] [PubMed]

56. Isozumi, H.; Kubota, K.; Tatara, R.; Horiba, T.; Hida, K.; Matsuyama, T.; Yasuno, S.; Komaba, S. Impact of Newly Developed Styrene-Butadiene-Rubber Binder on the Electrode Performance of High-Voltage LiNi$_{0.5}$Mn$_{1.5}$O$_4$ Electrode. *ACS Appl. Energy Mater.* **2020**, *3*, 7978–7987. [CrossRef]

57. Chou, W.Y.; Jin, Y.C.; Duh, J.G.; Lu, C.Z.; Liao, S.C. A Facile Approach to Derive Binder Protective Film on High Voltage Spinel Cathode Materials against High Temperature Degradation. *Appl. Surf. Sci.* **2015**, *355*, 1272–1278. [CrossRef]

58. Bigoni, F.; de Giorgio, F.; Soavi, F.; Arbizzani, C. Sodium Alginate: A Water-Processable Binder in High-Voltage Cathode Formulations. *J. Electrochem. Soc.* **2017**, *164*, A6171–A6177. [CrossRef]

59. Rao, L.; Jiao, X.; Yu, C.-Y.; Schmidt, A.; O'Meara, C.; Seidt, J.; Sayre, J.R.; Khalifa, Y.M.; Kim, J.-H. Multifunctional Composite Binder for Thick High-Voltage Cathodes in Lithium-Ion Batteries. *ACS Appl. Mater. Interfaces* **2022**, *14*, 861–872. [CrossRef]

60. Shin, M.; Song, W.J.; Han, J.G.; Hwang, C.; Lee, S.; Yoo, S.; Park, S.; Song, H.K.; Yoo, S.; Choi, N.S.; et al. Metamorphosis of Seaweeds into Multitalented Materials for Energy Storage Applications. *Adv. Energy Mater.* **2019**, *9*, 1900570. [CrossRef]

61. Zhong, H.; He, J.; Zhang, L. Better Cycle Stability and Rate Capability of High-Voltage LiNi$_{0.5}$Mn$_{1.5}$O$_4$ Cathode Using Water Soluble Binder. *Mater. Res. Bull.* **2017**, *93*, 194–200. [CrossRef]

62. Zhong, H.; Lu, J.; He, A.; Sun, M.; He, J.; Zhang, L. Carboxymethyl Chitosan/Poly(Ethylene Oxide) Water Soluble Binder: Challenging Application for 5 V LiNi$_{0.5}$Mn$_{1.5}$O$_4$ Cathode. *J. Mater. Sci. Technol.* **2017**, *33*, 763–767. [CrossRef]

63. Prosini, P.P.; Carewska, M.; Masci, A. A High Voltage Cathode Prepared by Using Polyvinyl Acetate as a Binder. *Solid. State Ion.* **2015**, *274*, 88–93. [CrossRef]

64. Pieczonka, N.P.W.; Borgel, V.; Ziv, B.; Leifer, N.; Dargel, V.; Aurbach, D.; Kim, J.H.; Liu, Z.; Huang, X.; Krachkovskiy, S.A.; et al. Lithium Polyacrylate (LiPAA) as an Advanced Binder and a Passivating Agent for High-Voltage Li-Ion Batteries. *Adv. Energy Mater.* **2015**, *5*, 1501008. [CrossRef]

65. Hitomi, S.; Kubota, K.; Horiba, T.; Hida, K.; Matsuyama, T.; Oji, H.; Yasuno, S.; Komaba, S. Application of Acrylic-Rubber-Based Latex Binder to High-Voltage Spinel Electrodes of Lithium-Ion Batteries. *ChemElectroChem* **2019**, *6*, 5070–5079. [CrossRef]

66. Dong, T.; Zhang, H.; Ma, Y.; Zhang, J.; Du, X.; Lu, C.; Shangguan, X.; Li, J.; Zhang, M.; Yang, J.; et al. A Well-Designed Water-Soluble Binder Enlightening the 5 V-Class LiNi$_{0.5}$Mn$_{1.5}$O$_4$ Cathodes. *J. Mater. Chem. A Mater.* **2019**, *7*, 24594–24601. [CrossRef]

67. Tanabe, T.; Gunji, T.; Honma, Y.; Miyamoto, K.; Tsuda, T.; Mochizuki, Y.; Kaneko, S.; Ugawa, S.; Lee, H.; Ohsaka, T.; et al. Preparation of Water-Resistant Surface Coated High-Voltage LiNi$_{0.5}$Mn$_{1.5}$O$_4$ Cathode and Its Cathode Performance to Apply a Water-Based Hybrid Polymer Binder to Li-Ion Batteries. *Electrochim. Acta* **2017**, *224*, 429–438. [CrossRef]

68. Taghavizadeh Yazdi, M.E.; Nazarnezhad, S.; Mousavi, S.H.; Sadegh Amiri, M.; Darroudi, M.; Baino, F.; Kargozar, S. Gum Tragacanth (GT): A Versatile Biocompatible Material beyond Borders. *Molecules* **2021**, *26*, 1510. [CrossRef]

69. Nejatian, M.; Abbasi, S.; Azarikia, F. Gum Tragacanth: Structure, Characteristics and Applications in Foods. *Int. J. Biol. Macromol.* **2020**, *160*, 846–860. [CrossRef]

70. Verma, C.; Pathania, D.; Anjum, S.; Gupta, B. Smart Designing of Tragacanth Gum by Graft Functionalization for Advanced Materials. *Macromol. Mater. Eng.* **2020**, *305*, 1900762. [CrossRef]

71. Barak, S.; Mudgil, D.; Taneja, S. Exudate Gums: Chemistry, Properties and Food Applications—A Review. *J. Sci. Food Agric.* **2020**, *100*, 2828–2835. [CrossRef]

72. Mohan, R.; Singh, S.; Kumar, G.; Srivastava, M. Evaluation of Gelling Behavior of Natural Gums and Their Formulation Prospects. *Indian J. Pharm. Educ. Res.* **2020**, *54*, 1016–1023. [CrossRef]

73. Verbeken, D.; Dierckx, S.; Dewettinck, K. Exudate Gums: Occurrence, Production, and Applications. *Appl. Microbiol. Biotechnol.* **2003**, *63*, 10–21. [CrossRef]

74. Fattahi, A.; Petrini, P.; Munarin, F.; Shokoohinia, Y.; Golozar, M.A.; Varshosaz, J.; Tanzi, M.C. Polysaccharides Derived from Tragacanth as Biocompatible Polymers and Gels. *J. Appl. Polym. Sci.* **2013**, *129*, 2092–2102. [CrossRef]

75. Versaci, D.; Nasi, R.; Zubair, U.; Amici, J.; Sgroi, M.; Dumitrescu, M.A.; Francia, C.; Bodoardo, S.; Penazzi, N. New Eco-Friendly Low-Cost Binders for Li-Ion Anodes. *J. Solid. State Electrochem.* **2017**, *21*, 3429–3435. [CrossRef]

76. Scalia, A.; Zaccagnini, P.; Armandi, M.; Latini, G.; Versaci, D.; Lanzio, V.; Varzi, A.; Passerini, S.; Lamberti, A. Tragacanth Gum as Green Binder for Sustainable Water-Processable Electrochemical Capacitor. *ChemSusChem* **2021**, *14*, 356–362. [CrossRef] [PubMed]

77. Sadat Hosseini, M.; Hemmati, K.; Ghaemy, M. Synthesis of Nanohydrogels Based on Tragacanth Gum Biopolymer and Investigation of Swelling and Drug Delivery. *Int. J. Biol. Macromol.* **2016**, *82*, 806–815. [CrossRef]

78. Veeramachineni, A.K.; Sathasivam, T.; Paramasivam, R.; Muniyandy, S.; Pushpamalar, J. Synthesis and Characterization of a Novel PH-Sensitive Aluminum Crosslinked Carboxymethyl Tragacanth Beads for Extended and Enteric Drug Delivery. *J. Polym. Environ.* **2019**, *27*, 1516–1528. [CrossRef]

79. Kurt, A. Physicochemical, rheological and structural characteristics of alcohol precipitated fraction of gum tragacanth. *Food Health* **2018**, *4*, 183–193. [CrossRef]

80. Sharma, B.; Thakur, S.; Trache, D.; Yazdani Nezhad, H.; Thakur, V.K. Microwave-Assisted Rapid Synthesis of Reduced Graphene Oxide-Based Gum Tragacanth Hydrogel Nanocomposite for Heavy Metal Ions Adsorption. *Nanomaterials* **2020**, *10*, 1616. [CrossRef]

81. Nowrouzi, I.; Khaksar Manshad, A.; Mohammadi, A.H. Effects of Tragacanth Gum as a Natural Polymeric Surfactant and Soluble Ions on Chemical Smart Water Injection into Oil Reservoirs. *J. Mol. Struct.* **2020**, *1200*, 127078. [CrossRef]

82. Indana, M.K.; Gangapuram, B.R.; Dadigala, R.; Bandi, R.; Guttena, V. A Novel Green Synthesis and Characterization of Silver Nanoparticles Using Gum Tragacanth and Evaluation of Their Potential Catalytic Reduction Activities with Methylene Blue and Congo Red Dyes. *J. Anal. Sci. Technol.* **2016**, *7*, 19. [CrossRef]

83. Wu, X.; Xing, Z.; Hu, Y.; Zhang, Y.; Sun, Y.; Ju, Z.; Liu, J.; Zhuang, Q. Effects of Functional Binders on Electrochemical Performance of Graphite Anode in Potassium-Ion Batteries. *Ionics* **2019**, *25*, 2563–2574. [CrossRef]

84. Dienwiebel, I.; Diehl, M.; Heidrich, B.; Yang, X.; Winter, M.; Börner, M. Enabling Aqueous Processing for $LiNi_{0.5}Mn_{1.5}O_4$-Based Positive Electrodes in Lithium-Ion Batteries by Applying Lithium-Based Processing Additives. *Adv. Energy Sustain. Res.* **2021**, *2*, 2100075. [CrossRef]

85. Ammundsen, B.; Jones, D.J.; Rozière, J.; Burns, G.R. Effect of Chemical Extraction of Lithium on the Local Structure of Spinel Lithium Manganese Oxides Determined by X-Ray Absorption Spectroscopy. *Chem. Mater.* **1996**, *8*, 2799–2808. [CrossRef]

86. Demeaux, J.; Caillon-Caravanier, M.; Galiano, H.; Lemordant, D.; Claude-Montigny, B. $LiNi_{0.4}Mn_{1.6}O_4$/Electrolyte and Carbon Black/Electrolyte High Voltage Interfaces: To Evidence the Chemical and Electronic Contributions of the Solvent on the Cathode-Electrolyte Interface Formation. *J. Electrochem. Soc.* **2012**, *159*, A1880–A1890. [CrossRef]

87. Syzdek, J.; Marcinek, M.; Kostecki, R. Electrochemical Activity of Carbon Blacks in LiPF6-Based Organic Electrolytes. *J. Power Sources* **2014**, *245*, 739–744. [CrossRef]

88. Younesi, R.; Christiansen, A.S.; Scipioni, R.; Ngo, D.; Simonsen, S.B.; Edström, K.; Hjelm, J.; Norby, P. Analysis of the Interphase on Carbon Black Formed in High Voltage Batteries. *J. Electrochem. Soc.* **2015**, *162*, A1289–A1296. [CrossRef]

89. Salian, G.D.; Højberg, J.; Fink Elkjaer, C.; Tesfamhret, Y.; Hernández, G.; Lacey, M.J.; Younesi, R. Investigation of Water-Soluble Binders for $LiNi_{0.5}Mn_{1.5}O_4$-Based Full Cells. *ChemistryOpen* **2022**, *11*, e202200065. [CrossRef]

90. Charles-Blin, Y.; Todoki, H.; Zettsu, N.; Teshima, K. Molecular Gate Effects Observed in Fluoroalkylsilane Self-Assembled Monolayers Grafted on $LiNi_{0.5}Mn_{1.5}O_4$ Cathodes: An Application to Efficient Ion-Exchange Reactions. *Mater. Adv.* **2021**, *2*, 5406–5414. [CrossRef]

91. Huang, B.; Wang, M.; Zhang, X.; Xu, G.; Gu, Y. Optimized Preparation of $LiNi_{0.6}Mn_{0.2}Co_{0.2}O_2$ with Single Crystal Morphology Cathode Material for Lithium-Ion Batteries. *Ionics* **2020**, *26*, 2689–2698. [CrossRef]

92. Pritzl, D.; Bumberger, A.E.; Wetjen, M.; Landesfeind, J.; Solchenbach, S.; Gasteiger, H.A. Identifying Contact Resistances in High-Voltage Cathodes by Impedance Spectroscopy. *J. Electrochem. Soc.* **2019**, *166*, A582–A590. [CrossRef]

93. Duncan, H.; Abu-Lebdeh, Y.; Davidson, I.J. Study of the Cathode–Electrolyte Interface of $LiMn_{1.5}Ni_{0.5}O_4$ Synthesized by a Sol–Gel Method for Li-Ion Batteries. *J. Electrochem. Soc.* **2010**, *157*, A528. [CrossRef]

94. Xu, Y.-H.; Zhao, S.-X.; Deng, Y.-F.; Deng, H.; Nan, C.-W. Improved Electrochemical Performance of 5 V Spinel $LiNi_{0.5}Mn_{1.5}O_4$ Microspheres by F-Doping and Li_4SiO_4 Coating. *J. Mater.* **2016**, *2*, 265–272. [CrossRef]

95. Scott, S.; Terreblanche, J.; Thompson, D.L.; Lei, C.; Hartley, J.M.; Abbott, A.P.; Ryder, K.S. Gelatin and Alginate Binders for Simplified Battery Recycling. *J. Phys. Chem. C* **2022**, *126*, 8489–8498. [CrossRef]

96. Zohuriaan-Mehr, M.J.; Mohamadnia, Z.; Kabiri, K.; Razavi-Nouri, M. Tragacanth Gum-Graft-Polyacrylonitrile: Synthesis, Characterization and Hydrolysis. *J. Polym. Res.* **2008**, *15*, 173–180. [CrossRef]

97. Nguyen, B.P.N.; Mariage, N.; Fredon, R.; Kelder, E.M.; Lestriez, B. Manufacturing of $LiNi_{0.5}Mn_{1.5}O_4$ Positive Composite Electrodes with Industry-Relevant Surface Capacities for Lithium Ion-Cells. *J. Electrochem. Soc.* **2015**, *162*, A1451–A1459. [CrossRef]